Materials
Horizons

Accepted Manuscript

This article can be cited before page numbers have been issued, to do this please use: F. Tallia, L. Russo, S. Li, A. L.H. Orrin, X. Shi, S. Chen, J. A.M. Steele, S. Meille, J. Chevalier, P. D. Lee, M. M. Stevens, L. Cipolla and J. R. Jones, *Mater. Horiz.*, 2018, DOI: 10.1039/C8MH00027A.

Volume 3 Number 1 January 2016 Pages 1–84

Materials Horizons

rsc.li/materials-horizons

ISSN 2051-6347

ROYAL SOCIETY OF CHEMISTRY

COMMUNICATION
Stefan A. F. Bon *et al.*
Control of vesicle membrane permeability with catalytic particles

175 YEARS

View Article Online
DOI: 10.1039/C8MH00027A

Journal: **Materials Horizons**
Article type: **Communication**

Bouncing and 3D Printable Hybrids with Self-healing Properties

Francesca Tallia[a], Laura Russo[b], Siwei Li[a,c], Alexandra L.H. Orrin[a,1], Xiaomeng Shi[a,d], Shu Chen[a,2], Joseph A.M. Steele[e], Sylvain Meille[f], Jérôme Chevalier[f], Peter D. Lee[d,g], Molly M. Stevens[a,c,e,h], Laura Cipolla[b,*], Julian R. Jones[a,*]

[a] *Department of Materials, Imperial College London, South Kensington Campus, London, SW7 2AZ, UK*

[b] *Department of Biotechnology and Biosciences, University of Milano-Bicocca, Piazza della Scienza 2, Milano, 20126, Italy*

[c] *Department of Bioengineering, Imperial College London, South Kensington Campus, London, SW7 2AZ, UK*

[d] *Research Complex at Harwell, Rutherford Appleton Laboratory, Harwell, Oxfordshire, OX11 0FA, UK*

[e] *Department of Medical Biochemistry and Biophysics, Karolinska Institutet, Scheeles väg 2, 17177 Stockholm, Sweden*

[f] *Université de Lyon, INSA Lyon, MATEIS CNRS UMR5510, Villeurbanne, F-69621, France*

[g] *School of Materials, The University of Manchester, Oxford Road, Manchester, M13 9PL, UK*

[h] *Institute of Biomedical Engineering, Imperial College London, South Kensington Campus, London, SW7 2AZ, UK*

* Corresponding Authors: julian.r.jones@imperial.ac.uk, laura.cipolla@unimib.it

---

[1] Present address: Withers & Rogers LLP, 4 More London Riverside, London, SE1 2AU, UK

[2] Present address: Crystallography, Department of Biological Sciences and ISMB, University of London, Malet Street, London, WC1E 7HX, UK

View Article Online
DOI: 10.1039/C8MH00027A

Conceptual insights

Conventional or even modern high tech glass is brittle and does not self-heal, while conventional composites often do not achieve true synergy of their component parts. Our solution is a new triple network hybrid material with a unique combination of elastomeric “bouncy” behaviour and autonomous intrinsic self-healing ability, while being able to biodegrade. Our transparent hybrid provides bouncy behaviour that can self-heal within seconds of fracture, without external stimulus, particularly if the fracture is internal. A new synthesis method was discovered that can lead to a new class of hybrid materials not possible to achieve by other means. Additive Manufacturing and 3D printing are popular, but the types of material that can be printed are limited. Our hybrid can be used directly as an ink for 3D printing (without use of additional binders). One application for our 3D printed hybrids is cartilage regeneration. Cartilage is not good at repairing itself and no implant biomaterials that can match the properties of articular cartilage are available to surgeons. Our 3D printed hybrids can act as temporary templates (scaffolds) that provoke articular cartilage matrix production from cartilage cells *in vitro*, indicating that true regeneration of articular cartilage may be possible.

View Article Online
DOI: 10.1039/C8MH00027A

Journal: **Materials Horizons**
Article type: **Communication**

Bouncing and 3D Printable Hybrids with Self-healing Properties

Francesca Tallia[a], Laura Russo[b], Siwei Li[a,c], Alexandra L.H. Orrin[a,1], Xiaomeng Shi[a,d], Shu Chen[a,2], Joseph A.M. Steele[e], Sylvain Meille[f], Jérôme Chevalier[f], Peter D. Lee[d,g], Molly M. Stevens[a,c,e,h], Laura Cipolla[b,*], Julian R. Jones[a,*]

[a] *Department of Materials, Imperial College London, South Kensington Campus, London, SW7 2AZ, UK*

[b] *Department of Biotechnology and Biosciences, University of Milano-Bicocca, Piazza della Scienza 2, Milano, 20126, Italy*

[c] *Department of Bioengineering, Imperial College London, South Kensington Campus, London, SW7 2AZ, UK*

[d] *Research Complex at Harwell, Rutherford Appleton Laboratory, Harwell, Oxfordshire, OX11 0FA, UK*

[e] *Department of Medical Biochemistry and Biophysics, Karolinska Institutet, Scheeles väg 2, 17177 Stockholm, Sweden*

[f] *Université de Lyon, INSA Lyon, MATEIS CNRS UMR5510, Villeurbanne, F-69621, France*

[g] *School of Materials, The University of Manchester, Oxford Road, Manchester, M13 9PL, UK*

[h] *Institute of Biomedical Engineering, Imperial College London, South Kensington Campus, London, SW7 2AZ, UK*

* Corresponding Authors: julian.r.jones@imperial.ac.uk, laura.cipolla@unimib.it

---

[1] Present address: Withers & Rogers LLP, 4 More London Riverside, London, SE1 2AU, UK

[2] Present address: Crystallography, Department of Biological Sciences and ISMB, University of London, Malet Street, London, WC1E 7HX, UK

View Article Online
DOI: 10.1039/C8MH00027A

Abstract

Conventional composites often do not represent true synergy of their constituent materials. This is particularly evident in biomaterial applications where devices must interact with cells, resist cyclic loads and biodegrade safely. Here we propose a new hybrid system, with co-networks of organic and inorganic components, resulting in unprecedented mechanical properties, including "bouncy" elasticity and intrinsic ability to self-heal autonomously. They are also developed as new 'inks' that can be directly 3D printed. A hybrid is different from a nanocomposite because the components are indistinguishable from each other at the nanoscale and above. The properties are generated by a novel methodology that combines *in situ* cationic ring-opening polymerisation with sol-gel, creating silica/poly-tetrahydrofuran/poly-ε-caprolactone hybrids with molecular scale interactions and covalent links. Cartilage is notoriously difficult to repair and synthetic biomaterials have yet to mimic it closely. We show that 3D printed hybrid scaffolds with pore channels of ~200 μm mimic the compressive behaviour of cartilage and provoke chondrocytes to produce markers integral to articular cartilage-like matrix. The synthesis method can be applied to different organic sources, leading to a new class of hybrid materials.

View Article Online
DOI: 10.1039/C8MH00027A

Introduction

Advanced materials are needed to fulfil the complex engineering design criteria for novel applications, where combinations of functional and mechanical properties are needed. Composites are used to combine the stiffness of one material, e.g. glass or carbon fibre, with the toughness of another, e.g. polymer matrix, but conventional composites generally fall short of full synergy of their constituent parts due to poor bonding at the interface between the components.[1]

The unique nanocomposite features of natural materials, such as bone and nacre,[1, 2] which have bonding and fine scale interactions between their inorganic and organic components, inspired the development of smart inorganic-organic hybrid materials with interpenetrating molecular co-networks of inorganic and organic components.[3-7] A hybrid is different from a nanocomposite because the components are indistinguishable from each other at the nanoscale and above, whereas in a nanocomposite, nanoparticles or fibres are discrete components dispersed in a polymer matrix. The fine scale interactions between the components in a hybrid have potential to create greater synergy as the hybrid can act as a single phase with congruent physicochemical behaviour and tailored mechanical properties.[4] Consequently, inorganic-organic hybrids could find diverse applications[5, 6] (electronics,[8] optical,[9] coatings,[10] biomedical,[11, 12] etc.).

The challenge is to synthesise hybrids that contain non-covalent interactions, that can be broken and re-formed, and strong covalent bonds, between the inorganic (usually silica) and polymeric chains. Structural hybrids are usually made by sol-gel processing,[6, 13] and covalent links can be formed through a "coupling agent", a molecule with both organic and inorganic functionalities that can act as a bridge between the two components. The use of polymers already containing siloxane groups ("Class II" hybrids) is limited only to those which are miscible in the sol-gel process. This problem can be overcome by forming both inorganic and organic phases *in situ* ("Class IV" hybrids), which allows a greater homogeneity and interpenetration of the two networks but requires the control over their simultaneous formation.[3, 4, 12]

Additive manufacturing can produce complex or custom-made shapes from digital designs or images.[14] Feasibility of using the sol to gel transition to directly 3D print a Class I (i.e. no covalent bonds between organic and inorganic components)[3, 4, 12] hybrid sol-gel "ink" was demonstrated by Gao

View Article Online
DOI: 10.1039/C8MH00027A

et al.[15] There are no examples of 3D printed Class II-IV hybrid objects. 3D printing is a leading technique to fabricate "scaffolds" for tissue regeneration,[16] which are porous structures that act as 3D temporary templates to support and guide the growth of native tissue. Articular cartilage regeneration is one of the most challenging fields, as no current surgical technique can regenerate articular cartilage and no current device can mimic its properties closely enough.

Herein we propose novel 3D printable silica/poly-tetrahydrofuran/poly-ε-caprolactone (SiO_2/PTHF/PCL-diCOOH) hybrid materials that show elastomeric behaviour and intrinsic autonomous self-healing ability, fabricated through an innovative methodology that combines sol-gel and an *in situ* cationic ring opening polymerisation (CROP) in mild conditions. It is this reaction that gave rise to the unusual mechanical properties.

Results and Discussion

Hybrid Synthesis

SiO_2/PTHF/PCL-diCOOH hybrids were successfully synthesised following a three-pot reaction depicted in Fig. 1a, which led to a combination of a Class II and Class IV hybrid with unprecedented properties. Common sol-gel processing involves ambient production of sol of hydrolysed alkoxide, such as tetraethyl orthosilicate (TEOS), the products of which undergo polycondensation to form a silicate gel network. Addition of the polymer at the sol stage allows formation of interpenetrating inorganic and organic co-networks.

Class II hybrids were previously made using an organosilane coupling agent ((3-glycidoxypropyl)trimethoxysilane, GPTMS), where the carboxylic groups of the polymer, e.g. gelatin, opened the epoxide ring of the GPTMS, so that the gelatin presented siloxane groups to the silica sol.[11] GPTMS was also used as coupling agent in Class II borophosphosilicate/PCL hybrids, where trimethyl borate catalysed the reaction between the epoxide ring and –OH groups of PCL-diol in toluene.[17] A co-polymer of caprolactone-GTPMS was recently synthesised for incorporation into hybrids[18] and (3-isocyanatopropyl)triethoxysilane (ICPTS) is an alternative coupling agent for PCL-containing Class II hybrids.[19-23]

Here, PCL-diol (M_n = 530 Da) was oxidised (TEMPO oxidation) to produce PCL-diCOOH,

View Article Online
DOI: 10.1039/C8MH00027A

presenting –COOH groups for reaction with GPTMS in tetrahydrofuran (THF). Interestingly, the epoxide ring of the GPTMS also acted as an initiator for polymerisation, resulting in *in situ* CROP of a fraction of the solvent (THF), generating poly-tetrahydrofuran (PTHF) as a second organic phase. This represents an innovative polymerisation process that occurs rapidly at room temperature and pressure (R.T.P.) and that is initiated by the activation of an epoxide ring by a catalyst (boron trifluoride diethyletherate, $BF_3 \cdot OEt_2$). The comparison of proton nuclear magnetic resonance (^{1}H-NMR) spectra, obtained on the organic precursor solution (containing THF, GPTMS and PCL-diCOOH) before and after the addition of $BF_3 \cdot OEt_2$ (Fig. 1b), showed that the three peaks corresponding to GPTMS epoxide ring disappeared after the addition of the catalyst, demonstrating complete opening of the epoxide rings.[24, 25] Concurrently, two new peaks given by the resonance of the methylene groups of PTHF[26] emerged at lower chemical shifts to the THF peaks. ^{1}H-NMR investigation also demonstrated that THF polymerisation does not occur without the addition of either $BF_3 \cdot OEt_2$ or GPTMS, but does not require the presence of PCL-diCOOH (Fig. S1). Hence, the proposed mechanism of reaction is schematised in Fig. 1c: because of the higher ring strain of oxirane (27.28 kcal mol^{-1}) compared to THF (5.63 kcal mol^{-1}),[27] $BF_3 \cdot OEt_2$ firstly activates ring opening of the GPTMS epoxide, through the corresponding intermediate 1 (step I, Fig. 1c). Subsequently, nucleophilic attack by the THF oxygen on intermediate 1 affords intermediate 2 and initiates the CROP (step II, Fig. 1c) and chain elongation steps (steps III-IV, Fig. 1c), resulting in a covalent bond between PTHF and GPTMS. PCL-diCOOH may act as quencher of the oxonium ion intermediates (steps V-VI, Fig. 1c).[24, 28, 29] A schematic of the hypothesised interactions among all components is included in Fig. 1c (intermediate 5) and how they are likely to combine as a hybrid is proposed in Fig. 1d. Further experiments consisting of the individual substitution of THF, GPTMS and $BF_3 \cdot OEt_2$ with a corresponding reagent with similar functionality showed that this CROP mechanism could be applied to other solvents (i.e. cyclic monomers) in the presence of an epoxide ring and a suitable Lewis acid as catalyst (Fig. S2). Therefore, this methodology potentially allows the preparation of new hybrids containing organic phases that are not miscible in the sol-gel process if pre-polymerised.

Hybrids in the shape of discs (Ø ≥ 80 mm, thickness = 0.6-2 mm) were obtained. Five different compositions were investigated through varying the initial TEOS/PCL-diCOOH ratio from 0/100 to

View Article Online
DOI: 10.1039/C8MH00027A

90/10 wt.%. The corresponding acronyms and final inorganic/organic (I/O) ratios measured through thermogravimetric analysis (TGA, Fig. S3) are reported in Table 1. All were transparent (Fig. 2a) and appeared homogeneous. Homogeneity at the nanoscale was confirmed by high resolution electron microscopy (Fig. 1d inset, Fig. S4a-b), where no distinction between the organic and the inorganic phases was detected, while the presence of the components was verified through electron dispersive X-ray spectrometry on different points of the analysed surface, which showed no significant variations of elemental ratios along a line scan (Fig. S4c-d). These observations, in combination with Fourier-transform infrared (FTIR) spectroscopy confirming the presence of SiO_2, PTHF and PCL-diCOOH (Fig. S5), proved the materials were homogeneous hybrids of three co-networks that were indistinguishable above the nanoscale.

Mechanical Properties of Hybrid Monoliths

The simultaneous bottom-up formation of silica and PTHF, allowed the production of large glass-based hybrid monoliths with unprecedented properties. The hybrid discs could be bent without breaking or permanently deforming (Fig. 2b), showing high flexibility, which increased as the organic content increased. The hybrids showed elastomeric deformation under tension (Fig. 2c, Fig. S6) and the ability to recover the initial shape when the load was released, until fracture. As inorganic content increased from 2.5 wt.% to 39 wt.%, true strain (ε^*) to failure decreased from 25.5 ± 3.3 % to 2.4 ± 1.5 % and true stress (σ^*) to failure increased from 0.12 ± 0.05 MPa to 1.42 ± 0.47 MPa (Fig. 2d), consistent with the expectation that, as the organic fraction decreases, the material becomes stronger but less flexible. This peculiar mechanical behaviour provides the hybrid with the ability to bounce (Video S1). Since the range of compositions showed a diverse range of mechanical properties and modes of deformation, Dynamic Mechanical Analysis (DMA) in tension was performed from 0 to 20% of the strain at failure, where the stress-strain curve was approximated as elastic (linear), to determine the minimum stiffness of the samples and their response to dynamic loading. The storage modulus (E') was at least 1 order of magnitude higher than the loss modulus (E'') for all compositions (tested at 1 Hz (Fig. 2e), representative of the 0.01-10 Hz frequency range investigated); the two moduli and the loss tangent ($tan(\delta)$, equal to the E''/E' ratio), were approximately constant. Very low values of $tan(\delta)$ were measured (< 0.07): since $tan(\delta)$ represents the relative contribution of the

View Article Online
DOI: 10.1039/C8MH00027A

dissipative vs. elastic contribution, the elastic nature of the hybrids and the absence of plastic deformation in the investigated strain range was confirmed. When deformation is elastic, *E'* gives an indication of stiffness and was used to compare different hybrid compositions. *E'* increased from 0.43 ± 0.16 MPa to 132 ± 15 MPa as inorganic content increased from 2.5 wt.% to 39 wt.%, demonstrating that the mechanical properties of the hybrid can be finely tailored through the I/O ratio, from rubber-like to glass-like behaviour with reduced brittleness, without varying the synthesis protocol and the chemistry.

The mechanical properties gave further evidence of the key role of THF polymerisation in the complex hybrid system. PTHF is a waxy polymer with very low melting point, which is better known to be exploited as soft segment in the production of many commercial elastomers, like polyester and polyurethane elastomers (e.g. Hytrel®, Spandex fibres).[30, 31] Here, it is believed that the *in situ* formation of PTHF within the hybrid system containing SiO_2 and PCL-diCOOH acts in a similar manner, determining the formation of a unique class of glass-based materials with elastomeric properties. No literature was found on a tri-component hybrid system containing both PCL and PTHF, only examples of Class II hybrids containing one of the two polymers functionalised with ICPTS are available for comparison. In both cases, hybrids failed at higher stresses than those reported here; e.g. SiO_2/PCL hybrids with an estimated ~17 wt.% SiO_2 failed at 21 MPa with strain ~50 %;[23] SiO_2/PTHF hybrids with an estimated ~40 wt.% SiO_2 failed at 11.5 MPa with strain ~29 %.[32] However, the deformation was mainly plastic with no sign of recovery. The ability to recover the deformation, shown by our SiO_2/PTHF/PCL-diCOOH hybrids, is an important requirement for materials to be used in different applications, especially those subjected to cyclic loads; e.g. biomaterials for cartilage regeneration.

Self-healing Ability

When internal cracks were artificially introduced in SiO_2/PTHF/PCL-diCOOH monoliths, the hybrids healed. Certain hybrid compositions even self-repaired when two opposing surfaces were placed back in contact after being cut through. When Si0-CL was cut into two pieces, with a sharp blade, the two pieces could be rejoined (Video S2). Optical microscopy images immediately after creating a crack and after a period of healing at R.T. are shown in Fig. 3a. Si0-CL, Si60-CL and Si70-CL showed some

View Article Online
DOI: 10.1039/C8MH00027A

degree of healing within 5 s, with healing occurring faster and to a greater extent as the organic content increased. A crack was still visible for Si70-CL, but a significant degree of recovery was observed from the initial defect. For higher silica contents (Si80-CL and Si90-CL), self-repair required 24 h to occur. Si80-CL healed more rapidly than Si90-CL. The degree of healing decreased as the time elapsed before putting the two cut surfaces back together increased. Using Si0-CL, SEM imaging (Fig. 3b-d) captured the healing process in a defect that was allowed to heal only partially, by bringing together the two fracture surfaces so that only the lower portions were in contact, showing crack bridging, mimicking bridging toughening mechanisms by organic fibrils seen in natural tissues, e.g. bone.[33] Si0-CL hybrids were then used to quantify the self-healing efficiency, where the fractured pieces were brought back together immediately after tensile fracture, and left at R.T. and humidity of ~50 % for 24 h and then re-tested in tension. Fig. 3e shows a typical variation in the σ^*-ε^* graph between the fresh sample and the sample tested after 24 h healing. The healing efficiency (η) of Si0-CL was calculated as the percentage of recovery of its original true strain and stress at failure, resulting equal to 36 ± 16 % and 31 ± 15 %, respectively.

Hybrid compositions with up to 39 wt.% SiO_2 possessed self-healing ability, which occurred faster and to a greater extent as inorganic content decreased, indicating the organic phase was responsible for the self-healing. Healing was autonomous, with no external stimuli (such as heat or light) required, and intrinsic, because no healing agents were embedded in the system.[34]

Self-healing materials have the ability to repair damage and recover their function using resources inherently available to the system.[34, 35] Healing triggered by external stimulus, e.g. heat, has been thoroughly studied,[36-38] but there are few examples of autonomous healable polymers because the healing derives from supramolecular interactions (e.g. hydrogen bonding).[39] Autonomous self-healing would ensure rapid recovery, but materials with intrinsic healing ability are difficult to design and manufacture.[34] To the best of the authors' knowledge, no inorganic-organic hybrid materials with autonomous self-healing properties have been reported. Certain polymers exhibit autonomous and intrinsic self-healing behaviour, usually based on the ability of destroying and re-forming chemical bonds related to weak non-covalent (i.e. supramolecular) interactions,[39-43] e.g. electrostatic forces, hydrogen bonding, ionic bonding, molecular diffusion. Recently, materials able to self-heal at low

View Article Online
DOI: 10.1039/C8MH00027A

temperature (i.e. at maximum 37°C) based on dynamic covalent bonds were described,[44, 45] but not in a hybrid.

We believe the self-healing behaviour of the SiO_2/PTHF/PCL-diCOOH hybrids is due to reversible intermolecular forces between organic components.[40, 46] The structure and functional groups of the components mean interactions to be considered are interchain intermolecular forces: London forces and dipole-dipole interactions among polymer chains (PTHF and PCL-diCOOH), plus hydrogen bonding due to the carboxyl groups of PCL (Fig. 1c, Fig. 1d). The hydrogen bonds are likely to be the strongest forces[47] and when PCL-diCOOH was not included in the reaction (Fig. S1c), the hybrid did not show self-healing capacity. While hydrogen bonding is thought to be essential for the self-healing, the highly elastomeric nature of the PTHF is important for chain rearrangements to accommodate the healing.[48, 49]

The specific combination of all the non-covalent bonding interactions could contribute to the organisation of the organic and inorganic moieties in an ordered way that is believed to be responsible for the autonomous and intrinsic self-healing process. Cutting the hybrid will break covalent bonds and other intermolecular interactions. It is likely that the recovery process was due to the “healing” of the non-covalent bonds and tensile strength was lower because the covalent bonds did not heal. Evidence to support this hypothesis is that the self-healing was most effective when the time of exposure to the air of the fractured surfaces was minimised. Moisture may interefere in hydrogen bonding among material components, limiting the healing process. The PTHF was key to these interactions as self-healing ability also decreased when the amount of silica increased.

Some self-healing materials have been found to be susceptible to creep and stress-relaxation and their mechanical stability was increased by the addition of permanent crosslinks at the expense of healing efficiency.[50] Stress-relaxation tests were performed on our Si0-CL (highest self-healing ability) and Si80-CL (the composition used for 3D printing of scaffolds) hybrids, showing that the relative stress loss was small and occurred over a sustained period (Fig. S7), confirming that the hybrids had good stability under prolonged tensile stress. The stability is consistent with the high number of covalent bonds between the inorganic and organic networks.

View Article Online
DOI: 10.1039/C8MH00027A

3D Printing of Scaffolds

Utilising the sol to gel transition of SiO_2/PTHF/PCL-diCOOH hybrid allowed it to be used as an “ink” for 3D computer-controlled additive manufacturing. Robotic-assisted 3D extrusion printing was used to fabricate porous scaffolds at R.T., following a grid-like pattern with aligned 90° layers (Fig. 4a, Video S3). The simultaneous ‘polymerisation’ of the organic and the inorganic phases and the covalent coupling mediated by GPTMS led to a gradual increase in viscosity of the ink for direct extrusion from the nozzles, with diameters as low as 200 μm and without the need of additives. Gelation was controlled such that during a window of time (“printing window”, ~ 1 h) the gel was fluid enough to flow smoothly through the nozzle and viscous enough to solidify and retain shape without collapsing on the printing bed. Each layer of gel was able to chemically bond to the previously deposited layer as the gelation reaction was on-going, leaving no sign of a discrete bonding interface (Fig. 4b). Si80-CL composition was chosen as the best compromise between flexibility and strength in the bulk state.

The scaffold architecture was investigated through X-ray microcomputed tomography (μCT) analysis, which allows quantification of strut and interconnected pore channel diameter (Fig. 4c).[51] The interconnections of the pore channels are visualised in Fig. 4d-e, where the local strut (Fig. 4d) and channel (Fig. 4e) diameters are shown. The modal interconnected channel size (Fig. 4f) was 130 ± 10 μm, with most channels in the range 40-240 μm and with strut diameters between 140-200 μm, consistent with the percentage porosity of 42 ± 4 % (measured through helium pycnometry). Channel sizes were confirmed by SEM images of the top surface and horizontal and vertical sections (Fig. 4g-i) of a Si80-CL scaffold. The top surface (Fig. 4g) and horizontal sections (Fig. 4h) had channel widths of ~200 μm but the vertical section (Fig. 4i) had channels with lower height than width, which was the reason behind the broad distribution found in the μCT analysis. Compressive testing on Si80-CL scaffolds showed that the elastomeric behaviour was preserved in the porous form (Fig. 5a); with mean stress ($|\sigma^*|$) and strain ($|\varepsilon^*|$) at failure of 1.2 ± 0.2 MPa and 36.0 ± 7.8 %, respectively. Si80-CL scaffolds were also tested under DMA within different ranges of strain. *E’* of the scaffolds at 1 Hz (representative of the 0.01-10 Hz frequency range investigated) was 5.1 ± 1.3 MPa, 7.2 ± 1.9

View Article Online
DOI: 10.1039/C8MH00027A

MPa, 8.7 ± 2.3 MPa for ε_c intervals of 1-5 %, 5-10 % and 10-15 %, respectively. The increase of *E'* as strain increased also confirmed the elastomeric behaviour of the scaffolds. As for bulk samples, very low values of *E''* and *tan(δ)* were measured, confirming the absence of plastic deformation in the investigated strain range. The storage modulus of Si80-CL scaffolds was slightly lower than it was for Si80-CL monoliths (23.6 ± 3.6 MPa, Fig. 2e), but was of the same order of magnitude. Therefore, while introducing pore channels reduced the stiffness of the bulk, the extrusion or layer-by-layer processing of 3D printing did not affect the inherent mechanical properties of the hybrid struts. The strain recovery observed in bulk samples was also maintained in scaffolds, as shown by cyclic testing (Fig. 5b). It is believed that an essential role is played by the covalent chemical bonding within the sol-gel, which guarantees the absence of an interface among struts and a continuum among stacked layers (Fig. 4b), allowing the scaffold to behave as a unique phase maintaining the hybrid bulk features. The 3D extrusion printing of sol-gel hybrids has only recently been explored through the printing of Class I silica/gelatin hybrid scaffolds with ~550 μm channel width and ~350 μm strut diameter.[15] Herein, remarkable progress was made because: (i) SiO_2/PTHF/PCL-diCOOH scaffolds were 3D printed without the need of additives or post-processing to stabilise the network; (ii) scaffolds with control on a finer scale were produced, reducing strut and channel size below ~200 μm.

Biodegradation and application in cartilage regeneration

PCL is known to be a biodegradable polyester through hydrolytic scission of the ester linkage.[52] Therefore, a preliminary biodegradation study was performed by soaking Si80-CL scaffolds in Phosphate Buffered Saline (PBS) solution for 7 days. The scaffolds did not show any visual damage during the immersion in PBS (Fig. S8a). This means that Si80-CL composition maintained a good balance between hydrophilic silica and hydrophobic organic phases that prevented scaffolds from swelling or cracking in the aqueous environment. After soaking for 7 days, the mass loss of the scaffolds was measured as the difference in mass before the test and when completely dried after soaking, resulting in a value of 14.5 ± 0.5 wt.%. The degradation products were then analysed with ^{1}H-NMR, which confirmed that the organic components released were the degradation products of PCL-diCOOH (Fig. S8b), with no PTHF detected in solution. No significant Si release was recorded by ICP-OES, as it never exceeded 2.7 μg mL^{-1}. Only organic phase was lost during immersion in PBS,

View Article Online
DOI: 10.1039/C8MH00027A

as supported by TGA (Fig. S8c): after the immersion for 7 days an increase in I/O ratio was measured, corresponding to a polymer loss of 12 wt.%, similar to the mean loss of 14.5 wt.% from scaffold mass measurements. Tian *et al.*[53] and Rhee *et al.*[22, 54] showed that the weight loss of silica-based hybrids containing PCL in PBS mostly came from the degradation of the PCL component, with negligible release from the silica phase. Pol *et al.* proved stability of PTHF in PBS over three months.[55] Thus it was expected that PCL-diCOOH was the only polymer degraded during the test.

No differences were seen in pore architecture from SEM images of the scaffolds (Fig. 4g-i), but some changes on the surface were observed above 1000× (Fig. S8d). While the pristine surface was completely smooth (Fig. S8d_1-d_2), the formation of small hackle-like features, usually seen in brittle fractures,[56] was visible after 7 days in PBS (Fig. S8d_3-d_4). This was found to be only a surface effect, since they were not observed in the inner part exposed by cutting a section (Fig. S8d_3). Hence, the partial release of PCL degradation products from the scaffolds during immersion in PBS was deemed to be surface degradation as it did not cause evident variations in the shape, volume or morphology of the scaffolds.

On immersion in PBS, a stiffening of the scaffold was noticed (Fig. 5a), with mean stress ($|\sigma^*|$) and strain ($|\varepsilon^*|$) at failure of 1.2 ± 0.2 MPa and 25.2 ± 4.4 %. Soaked scaffolds showed a reduction of ~10 % in strain at failure, but maintained the same compressive strength as pre-soaking samples. This was an important finding because it showed that SiO_2/PTHF/PCL-diCOOH hybrids scaffolds did not exhibit a rapid loss of mechanical properties upon soaking, rather the mechanical properties were maintaned over degradation and only changed according to the variation in I/O ratio.

3D scaffolds with a network of interconnected pores have been extensively investigated as guide and support for tissue repair,[12, 16, 57, 58] but articular cartilage regeneration[59] is still an unmet clinical need. The combined effect of the graded structure and the distribution of the biological components and fluids makes articular cartilage an extraordinary viscoelastic material with the ability to withstand a countless number of compression cycles.[59] It shows compressive strength of 22-37 MPa,[60, 61] with physiological activities applying stresses in the range 1-18 MPa,[62, 63] and maximum compressive strain in the range 24-28 %.[60, 61] Si80-CL hybrid scaffolds successfully showed a non-linear elastomeric deformation with the ability to recover the deformation, mimicking the behaviour of native cartilage

View Article Online
DOI: 10.1039/C8MH00027A

with comparable failure strain (from ~36 to ~25 % over 7 days in PBS). The failure stress (~1.2 MPa) is lower than the one reported for cartilage, being positioned at the lower limit of the range of physiological stresses. The low compressive strength may limit the patients in their initial activities; however, the colonisation of the scaffold with newly formed cartilage would then add further support and guarantee enough mechanical properties *in vivo*. Improvement in the 3D printing process and design of pore architecture could increase mechanical properties further.

Cartilage Cell Studies

The combination of the 3D printed architecture of the SiO_2/PTHF/PCL-diCOOH hybrids and their mechanical behaviour suggests they could be suitable for articular cartilage regeneration. In sports injuries, the microfracture technique is used, where microfractures are punched into the underlying subchondral bone to release bone marrow containing stem cells. However, success of has been limited to the first two years following surgery due to fibrocartilage formation rather than highly organised articular (hyaline) cartilage[64]. *In vitro* cell cultures of ATDC5 cartilage cells in Si80-CL scaffolds suggest that the material has the ability not only to support robust cell attachment (Fig. 6a), viability and growth to fill pore structures (Fig. 6b), but also to induce chondrogenic differentiation and hyaline cartilaginous matrix formation, as evidenced by the robust expression of Sox9, Collagen Type II and Aggrecan (Fig. 6c-e), which are associated with high quality articular cartilage production. Images were taken of cross-sections through the middle of the 3D scaffolds. Importantly, hyaline-like matrix formation was preferential over production of other types of cartilage matrix, as the expression of Collagen Type I (fibrous cartilage) or Collagen Type X (ossification) was negligible (Fig. S9). When the cells were cultured on PCL scaffolds of similar architecture (pores 250 μm × 600 μm × ~100 μm h, Fig. S10), less Sox9, Collagen Type II and Aggrecan (Fig. 6f-h) were expressed compared to cells cultured on the hybrids. The results were confirmed by qPCR (cells cultured on Si80-CL scaffolds expressed significantly up-regulated *col2a1* and *aggrecan* genes) and quantitative dimethylmethylene blue (DMMB) assay (Fig. 6i-l). The improved synthesis of negatively charged sulfated glycosaminoglycan (GAG), which produces swelling pressure through interaction with the interstitial fluid[65], could potentially contribute to superior compressive stiffness of engineered tissue on Si80-CL scaffolds in comparison to conventional scaffold materials such as PCL. Improved cartilage matrix

View Article Online
DOI: 10.1039/C8MH00027A

formation on the hybrids is likely to be due to a number of factors including suitable surface chemistry, stiffness of the material and more importantly pore architecture, because chondrocytes cultured in excessively large pores are likely to experience environments similar to monolayer culture and undergo dedifferentiation, during which cells assume fibroblastic characteristics and lose their capacity to form hyaline cartilaginous tissue.[66-68] The silica component of the hybrid may also have provided improved cell recognition sites, which are absent in conventional PCL.[69] Therefore, SiO_2/PTHF/PCL-diCOOH scaffolds are promising alternatives for their use in skeletal tissue engineering.

Conclusions

In conclusion, we presented a novel hybrid synthesis that combines sol-gel with *in situ* CROP of THF in mild conditions. This allowed the production of SiO_2/PTHF/PCL-diCOOH hybrid materials with unprecedented versatile features: elastomeric “bouncy” behaviour, self-healing ability without any external trigger and suitable viscosity for 3D extrusion printing. The properties and the shape of the final device can be tailored with a view to the desired application by simply changing the inorganic/organic ratio and the printing design, leading to a new system with a great potential in applications such as self-healing coatings and 3D printed scaffolds for tissue regeneration. Biodegradation studies in PBS showed slow loss of PCL components. Encouraging results were obtained from *in vitro* chondrogenic differentiation, making SiO_2/PTHF/PCL-diCOOH scaffolds suitable candidates for articular cartilage regeneration. The innovative synthesis can be applied to other suitable monomers, paving the way to a new class of hybrid materials impossible to achieve by other means.

Data and material availability

Experimental section, supplementary figures and videos are available in Electronic supplementary information (ESI). Raw data is available on request from rdm-enquiries@imperial.ac.uk.

View Article Online
DOI: 10.1039/C8MH00027A

Conflict of Interest

The authors declare no conflict of interest.

Acknowledgements

The authors acknowledge the European Commission funding under the 7th Framework Programme (Marie Curie Initial Training Networks; grant number: 289958, Bioceramics for bone repair) and EPSRC (EP/M019950/1, EP/N025059/1 and EP/I02249X/1). The authors also gratefully acknowledge support from the Vetenskapsrädet grant 2015-02904. Dr Jesús Del Val Garcia (Applied Physics Department, University of Vigo, Spain; Department of Materials, Imperial College London, UK) is acknowledged for the editing of Video S1.

View Article Online
DOI: 10.1039/C8MH00027A

References

1. U. G. K. Wegst, H. Bai, E. Saiz, A. P. Tomsia and R. O. Ritchie, *Nat. Mater.*, 2015, **14**, 23-36.
2. A. R. Studart, *Adv. Mater.*, 2012, **24**, 5024-5044.
3. C. Sanchez and F. Ribot, *New J. Chem.*, 1994, **18**, 1007-1047.
4. B. M. Novak, *Adv. Mater.*, 1993, **5**, 422-433.
5. C. Sanchez, B. Julian, P. Belleville and M. Popall, *J. Mater. Chem.*, 2005, **15**, 3559-3592.
6. C. Sanchez, P. Belleville, M. Popall and L. Nicole, *Chem. Soc. Rev.*, 2011, **40**, 696-753.
7. G. Kickelbick, *Hybrid Mater.*, 2014, **1**, 39-51.
8. R. Plass, S. Pelet, J. Krueger, M. Grätzel and U. Bach, *J. Phys. Chem. B*, 2002, **106**, 7578-7580.
9. R. Houbertz, G. Domann, C. Cronauer, A. Schmitt, H. Martin, J. U. Park, L. Fröhlich, R. Buestrich, M. Popall, U. Streppel, P. Dannberg, C. Wächter and A. Bräuer, *Thin Solid Films*, 2003, **442**, 194-200.
10. G. Schottner, J. Kron and A. Deichmann, *J. Sol-Gel Sci. Technol.*, 1998, **13**, 183-187.
11. O. Mahony, O. Tsigkou, C. Ionescu, C. Minelli, L. Ling, R. Hanly, M. E. Smith, M. M. Stevens and J. R. Jones, *Adv. Funct. Mater.*, 2010, **20**, 3835-3845.
12. J. R. Jones, *Acta Biomater.*, 2013, **9**, 4457-4486.
13. C. Sanchez and M. In, *J. Non-Cryst. Solids*, 1992, **147**, 1-12.
14. J. A. Lewis, *Adv. Funct. Mater.*, 2006, **16**, 2193-2204.
15. C. Gao, M. N. Rahaman, Q. Gao, A. Teramoto and K. Abe, *J. Biomed. Mater. Res. A*, 2013, **101A**, 2027-2037.
16. Q. Fu, E. Saiz and A. P. Tomsia, *Adv. Funct. Mater.*, 2011, **21**, 1058-1063.
17. D. Mondal, A. S. Rizkalla and K. Mequanint, *RSC Adv.*, 2016, **6**, 92824-92832.
18. T. Sang, S. Li, H.-K. Ting, M. M. Stevens, C. R. Becer and J. R. Jones, *Chem. Mater.*, 2018, DOI: 10.1021/acs.chemmater.8b00751.
19. D. Tian, P. Dubois and R. Jérôme, *Polymer*, 1996, **37**, 3983-3987.
20. D. Tian, P. Dubois and R. Jérôme, *J. Polym. Sci. A Polym. Chem.*, 1997, **35**, 2295-2309.
21. D. Tian, S. Blacher, P. Dubois and R. Jérôme, *Polymer*, 1998, **39**, 855-864.
22. S.-H. Rhee, J.-Y. Choi and H.-M. Kim, *Biomaterials*, 2002, **23**, 4915-4921.
23. S.-H. Rhee, *Biomaterials*, 2004, **25**, 1167-1175.
24. L. Gabrielli, L. Connell, L. Russo, J. Jiménez-Barbero, F. Nicotra, L. Cipolla and J. R. Jones, *RSC Adv.*, 2014, **4**, 1841-1848.
25. L. Gabrielli, L. Russo, A. Poveda, J. R. Jones, F. Nicotra, J. Jiménez-Barbero and L. Cipolla, *Chem. Eur. J.*, 2013, **19**, 7856-7864.
26. J. Zhang, Y. Niu, C. Huang, L. Xiao, Z. Chen, K. Yang and Y. Wang, *Polym. Chem.*, 2012, **3**, 1390-1393.
27. A. J. Clark and S. S. Hoong, *Polym. Chem.*, 2014, **5**, 3238-3244.
28. O. Nuyken and S. Pask, *Polymers*, 2013, **5**, 361-403.

View Article Online
DOI: 10.1039/C8MH00027A

29. B. Köhler, W. Ebert, K. Horn, W. S. Schäfer, J. Kirsch, and R. Dhein, *US Patent 5633339*, 1997.

30. N. Barksby and S. D. Seneker, *US Patent 5545706*, 1996.

31. S. D. Seneker and B. D. Lawrey, *US Patent 5691441*, 1997.

32. N. Miyata, K.-i. Fuke, Q. Chen, M. Kawashita, T. Kokubo and T. Nakamura, *Biomaterials*, 2002, **23**, 3033-3040.

33. R. K. Nalla, J. H. Kinney and R. O. Ritchie, *Nat. Mater.*, 2003, **2**, 164-168.

34. B. J. Blaiszik, S. L. B. Kramer, S. C. Olugebefola, J. S. Moore, N. R. Sottos and S. R. White, *Annu. Rev. Mater. Res.*, 2010, **40**, 179-211.

35. E. B. Murphy and F. Wudl, *Progr. Polym. Sci.*, 2010, **35**, 223-251.

36. S. R. White, N. R. Sottos, P. H. Geubelle, J. S. Moore, M. R. Kessler, S. R. Sriram, E. N. Brown and S. Viswanathan, *Nature*, 2001, **409**, 794-797.

37. Y. Imai, H. Itoh, K. Naka and Y. Chujo, *Macromolecules*, 2000, **33**, 4343-4346.

38. S. Schäfer and G. Kickelbick, *Polymer*, 2015, **69**, 357-368.

39. F. Herbst, D. Döhler, P. Michael and W. H. Binder, *Macromol. Rapid Commun.*, 2013, **34**, 203-220.

40. Y. Chen, A. M. Kushner, G. A. Williams and Z. Guan, *Nat. Chem.*, 2012, **4**, 467-472.

41. P. Cordier, F. Tournilhac, C. Soulie-Ziakovic and L. Leibler, *Nature*, 2008, **451**, 977-980.

42. D. Montarnal, F. Tournilhac, M. Hidalgo, J.-L. Couturier and L. Leibler, *J. Am. Chem. Soc.*, 2009, **131**, 7966-7967.

43. J. Liu, C. S. Y. Tan, Z. Yu, N. Li, C. Abell and O. A. Scherman, *Adv. Mater.*, 2017, **29**, 1605325.

44. H. Ying, Y. Zhang and J. Cheng, *Nat. Commun.*, 2014, **5**, 3218.

45. A. Rekondo, R. Martin, A. Ruiz de Luzuriaga, G. Cabanero, H. J. Grande and I. Odriozola, *Mater. Horiz.*, 2014, **1**, 237-240.

46. G. M. L. v. Gemert, J. W. Peeters, S. H. M. Söntjens, H. M. Janssen and A. W. Bosman, *Macromol. Chem. Phys.*, 2012, **213**, 234-242.

47. N. Roy, E. Buhler and J.-M. Lehn, *Chem. Eur. J.*, 2013, **19**, 8814-8820.

48. D. Zhu, Q. Ye, X. Lu and Q. Lu, *Polym. Chem.*, 2015, **6**, 5086-5092.

49. A. Phadke, C. Zhang, B. Arman, C.-C. Hsu, R. A. Mashelkar, A. K. Lele, M. J. Tauber, G. Arya and S. Varghese, *Proc. Natl. Acad. Sci. U.S.A.*, 2012, **109**, 4383-4388.

50. J. J. Cash, T. Kubo, D. J. Dobbins and B. S. Sumerlin, *Polym. Chem.*, 2018, **9**, 2011-2020.

51. J. R. Jones, G. Poologasundarampillai, R. C. Atwood, D. Bernard and P. D. Lee, *Biomaterials*, 2007, **28**, 1404-1413.

52. M. A. Woodruff and D. W. Hutmacher, *Progr. Polym. Sci.*, 2010, **35**, 1217-1256.

53. D. Tian, P. Dubois, C. Grandfils, R. Jérôme, P. Viville, R. Lazzaroni, J.-L. Brédas and P. Leprince, *Chem. Mater.*, 1997, **9**, 871-874.

54. S.-H. Rhee, *Biomaterials*, 2003, **24**, 1721-1727.

55. B. J. M. Pol, L. van der Does, A. Bantjes and P. B. van Wachem, *J. Biomed. Mater. Res.*, 1996, **32**, 321-331.

56. J. J. Mecholsky, R. W. Rice and S. W. Freiman, *J. Am. Ceram. Soc.*, 1974, **57**, 440-443.

View Article Online
DOI: 10.1039/C8MH00027A

57. S. J. Hollister, *Nat. Mater.*, 2005, **4**, 518-524.

58. J. M. Sobral, S. G. Caridade, R. A. Sousa, J. F. Mano and R. L. Reis, *Acta Biomater.*, 2011, **7**, 1009-1018.

59. Z. Izadifar, X. Chen and W. Kulyk, *J. Funct. Biomater.*, 2012, **3**, 799-838.

60. R. Repo and J. Finlay, *J. Bone Joint Surg. Am.*, 1977, **59**, 1068-1076.

61. A. J. Kerin, M. R. Wisnom and M. A. Adams, *Proc. Inst. Mech. Eng. H*, 1998, **212**, 273-280.

62. L. S. Matthews, D. A. Sonstegard and J. A. Henke, *Acta Orthop. Scand.*, 1977, **48**, 511-516.

63. W. A. Hodge, K. L. Carlson, R. S. Fijan, R. G. Burgess, P. O. Riley, W. H. Harris and R. W. Mann, *J. Bone Joint Surg. Am.*, 1989, **71**, 1378-1386.

64. K. Mithoefer, T. McAdams, R. J. Williams, P. C. Kreuz and B. R. Mandelbaum, *Am. J. Sports Med.*, 2009, **37**, 2053-2063.

65. M. T. Bayliss, D. Osborne, S. Woodhouse and C. Davidson, *J. Biol. Chem.*, 1999, **274**, 15892-15900.

66. K. Pelttari, A. Winter, E. Steck, K. Goetzke, T. Hennig, B. G. Ochs, T. Aigner and W. Richter, *Arthritis Rheum.*, 2006, **54**, 3254-3266.

67. P. D. Benya and J. D. Shaffer, *Cell*, 1982, **30**, 215-224.

68. M. M. J. Caron, P. J. Emans, M. M. E. Coolsen, L. Voss, D. A. M. Surtel, A. Cremers, L. W. van Rhijn and T. J. M. Welting, *Osteoarthr. Cartil.*, 2012, **20**, 1170-1178.

69. J. Liao, Y. Qu, B. Chu, X. Zhang and Z. Qian, *Sci. Rep.*, 2015, **5**, 9879.

70. R. A. Shanks and I. Kong, in *Advances in Elastomers I: Blends and Interpenetrating Networks*, (eds. M. P. Visakh, S. Thomas, K. A. Chandra and P. A. Mathew), Springer Berlin Heidelberg, Berlin, Heidelberg, 2013, Ch. *General Purpose Elastomers: Structure, Chemistry, Physics and Performance* pp. 11-45.

71. S. Cantournet, R. Desmorat and J. Besson, *Int. J. Solids Struct.*, 2009, **46**, 2255-2264.

View Article Online
DOI: 10.1039/C8MH00027A

Figure Captions and Tables

Figure 1. SiO_2/PTHF/PCL-diCOOH hybrid synthesis: a, Flowchart of the synthesis protocol to prepare hybrid materials in form of monoliths (e.g. cylindrical sample (Ø = 9 mm, height = 10 mm) shown in the inset of D1 step) and 3D porous scaffolds (e.g. cubic scaffold of 8×8×8 mm shown in the inset of D2 step). **b**, Typical ^{1}H-NMR spectra in $CDCl_3$ of the solution containing organic precursors (step A in **a**) that show the effect of the addition of $BF_3{\cdot}OEt_2$, which catalyses the CROP reaction described in **c**. The spectrum at the bottom, obtained before $BF_3{\cdot}OEt_2$ addition, displays the characteristic peaks of the starting reagents (THF, GPTMS, PCL-diCOOH): the three peaks highlighted in the blue region (quartet at $\delta = 2.60$ ppm, triplet at $\delta = 2.77$ ppm and multiplet at $\delta = 3.13$ ppm) correspond to GPTMS epoxide ring. The spectrum at the top is obtained after 1.5 h from $BF_3{\cdot}OEt_2$ addition (before mixing with inorganic precursor solution): the peaks in the blue region are missing, demonstrating the completion of the opening of GPTMS' epoxide ring; this is combined with the appearance of PTHF peaks (multiplet at $\delta = 1.62$ and triplet at $\delta = 3.41$ ppm, orange regions), confirming the ring-opening polymerisation of THF. **c**, Reaction mechanism for cationic ring-opening polymerisation of THF; intermediate 5 includes the hypothesised interactions among organic components. **d**, Schematic of the SiO_2/PTHF/PCL-diCOOH hybrid material, demonstrating the hypothesised GPTMS-mediated covalent bonding between inorganic and organic components and interactions between polymer chains; inset: TEM image (scale bar = 50 nm) showing the homogeneity of the hybrid network at the nanoscale.

Figure 2. Mechanical properties of the SiO_2/PTHF/PCL-diCOOH hybrids in the bulk state: a, Example of Si80-CL hybrid disc (Ø = 90 mm, height = 2 mm); **b,** Manual bending of the Si80-CL disc shown in **a**; **c**, Uni-axial tensile testing of a rectangular specimen (25×10 mm; thickness = 0.6-2 mm) manually cut from a disc; **d**, Mean true stress (σ*) and true strain (ε*) at failure relative to the silica content (SiO_2 wt.%) as result of tensile testing; **e**, Storage modulus (E') and loss modulus (E'') relative to the silica content (SiO_2 wt.%) as result of DMA analysis in tension on the five hybrid compositions at 1 Hz. The inset shows the magnification of the results for Si0-CL, Si60-CL and Si70-CL. (see **Table 1** for correspondence SiO_2 wt.% - sample acronym). Error bars in **d** and **e** represent the standard deviation.

Figure 3. Autonomous and intrinsic self-healing ability: a, Optical microscope images of samples of the five hybrid compositions before creation of a defect (top) and after self-healing at R.T. (bottom). Rapid healing was observed for samples with silica content ≤ 17.4 wt.%, hence images for Si0-CL, Si60-CL and Si70-CL, were taken after only 5 s from defect creation; Si80-CL and Si90-CL showed a slower recovery, therefore images were taken after 24 h from defect creation. Scale bar = 500 μm. **b-c-**

View Article Online
DOI: 10.1039/C8MH00027A

d, SEM images of a defect created on a Si0-CL sample and allowed to heal only partially (i.e. only the lower portions of the opposing surfaces were put in contact when re-joined) to show the bridging effect along the fractured surfaces during the self-healing process. The margins of the defects are visible in **b** and a magnification of the bridging is reported in **c**; this behaviour was confirmed also on other areas of the sample (**d**). Scale bars: 50 μm in **b**; 10 μm in **c-d**. **e**, Typical stress-strain graph of quantitative self-healing tensile test on Si0-CL (true values of stress (σ*) and strain (ε*) were considered). It shows the comparison between the curve obtained from the fresh sample (‘Before self-healing’) up to failure and the curve obtained from the same sample after it has been fractured into two pieces, allowed to reattach for 24 h at R.T. and humidity of ~50 % and then re-tensile tested up to failure (‘After 24h self-healing’). The inserts display a typical Si0-CL sample going through this sequence.

Figure 4. 3D extrusion printed scaffolds: a, Example of a scaffold (8×8×8 mm), with a grid-like 3D porous structure with aligned 90° layers (obtained from the repetition of 2 orthogonal layers, each consisting of a linear array of parallel struts); **b**, SEM image of a horizontal section showing the interaction among struts belonging to three different layers (identified with “1-2-3” from the outer to the inner layer): the fusion between two adjoining struts is highlighted with a dashed line; **c**, Example μCT image (cubic child volume, dimensions 1235 μm) of a 3D printed Si80-CL scaffold, showing 3D rendering of the struts used for the μCT image analyses in **d** to **f**; **d** strut and **e** interconnecting channel thickness visualised illustrating connectivity coloured by local diameter that fits within the structure; **f**, Strut and interconnecting channel size distributions calculated from **d-e** and binned as a percentage of the total. Scaffold porosity of 40% was calculated from these distributions (within the 42 ± 4% measured with He pycnometry); **g- i**, SEM images of top surface, horizontal (x-y) section and vertical (z-y) section, respectively, of a 3D printed Si80-CL scaffold. Scale bars: 100 μm in **b**; 250 μm in **c-e**; 200 μm in **g-i**.

Figure 5. Compression testing on Si80-CL scaffolds: a, Typical true stress-strain graph (σ*-ε*) for a Si80-CL scaffold as prepared (“Pre-soaking”) and after soaking in PBS for a week (“After 7 days PBS”). Non-linear elastomeric behaviour was recorded until failure occurred; failure was identified by the dramatic change in the trend towards a horizontal fragmented graph due to the fracture of the different scaffold layers. A stiffening of the hybrid was observed upon soaking as consequence of the degradation of the polymer component (Fig. S8). Modulus of toughness (U_T), that represents the energy required to bring the sample to failure, was 142 kPa and 113 kPa for pre- and post-soaking tests, respectively; **b**, Typical cyclic loading conventional stress-strain (σ_c-ε_c) curves for a Si80-CL scaffold, showing its ability to recover the shape at the chosen level of strain. An anomalous first cycle is detected and is attributed to the combination of two effects: (i) The irreversible rupture of single labile struts, which are inherent in the not perfectly regular structure of the scaffold but were proven

View Article Online
DOI: 10.1039/C8MH00027A

not to affect the mechanical behaviour significantly. (ii) The Mullins Effect, a characteristic featured by pure elastomers, which is mechanical stress softening due to the transformation of hard domains to soft domains that determines a decrease in stress on unloading compared to loading, giving rise to hysteresis.[70, 71] This phenomenon occurs mostly in large strain cyclic loading tests in the first few cycles because of the sliding between elastomer macromolecular chains under mechanical stress, which causes the temporary elimination of hard domains present in the microstructure by removing entanglements in its internal structure. This effect is mostly recovered after the stress is removed, with the exception of some entanglements that cannot be recovered and are removed in the first few cycles.[71] The other nine cycles almost perfectly overlap, with a very small hysteresis.

Figure 6. *In vitro* cell studies on Si80-CL and PCL scaffolds: a, Immunohistochemical staining of cell nuclei (DAPI, blue fluorescence), Vimentin intermediate filaments (green fluorescence) and F-actin microfilaments (red fluorescence). Cells infiltrated the pore structure within the scaffold and expression of Vimentin and F-actin is evidence of functional cell adhesion. **b**, WST-1 assay of ATDC5 seeded Si80-CL scaffolds cultured for up to 14 days (n = 3). The gradual increase in optical density of WST-1 solution was evidence of on-going cell survival and continual cell growth on the scaffolds. **c-h**, Immunohistochemical analysis of day-21 ATDC5 seeded Si80-CL and PCL constructs with markers for cartilage-related proteins. Robust chondrogenic differentiation and hyaline cartilaginous matrix formation on Si80-CL scaffolds was confirmed by staining for Sox9 (marker for chondrogenic differentiation), Aggrecan (cartilage-specific proteoglycan) and Collagen Type II (a constituent of hyaline cartilage) (**c-e**). Hyaline cartilaginous matrix formation appeared suboptimal in PCL scaffolds (**f-h**). **i-k**, Analysis of expression of Sox9, Col2a1 and Aggrecan using real-time qPCR (n = 3) confirmed the observations from immunohistochemistry. There was negligible Collagen Type I (fibrocartilage marker) and X (hypertrophic cartilage marker) on either type of scaffolds (Fig. S9). **l**, DMMB assay demonstrated that cells cultured on Si80-CL scaffolds synthesised significantly more sGAG than those on PCL scaffolds. * $p<0.05$. Scale bars in **a**, **c-h** = 100 μm. Error bars in **b** and **l** represent the standard deviation, error bars in **i-k** represent range (upper and lower limits) of relative gene expression.

View Article Online
DOI: 10.1039/C8MH00027A

Table 1. Acronyms of the SiO_2/PTHF/PCL-diCOOH hybrid samples (1st column) and corresponding ratios between inorganic and organic components: the ratio between TEOS and PCL-diCOOH in the starting sol-gel reaction (2nd column); the actual values of I/O wt.% measured from TGA in the final hybrid samples (3rd column). When no TEOS is present (Si0-CL) the SiO_2 fraction is entirely due to GPTMS inorganic contribution.

Acronym	Starting TEOS/PCL-diCOOH wt.%	Final I/O wt.% (measured from TGA)
Si0-CL	0/100	2.5/97.5
Si60-CL	60/40	12.3/87.7
Si70-CL	70/30	17.4/82.6
Si80-CL	80/20	24.7/75.3
Si90-CL	90/10	38.7/61.3

View Article Online
DOI: 10.1039/C8MH00027A

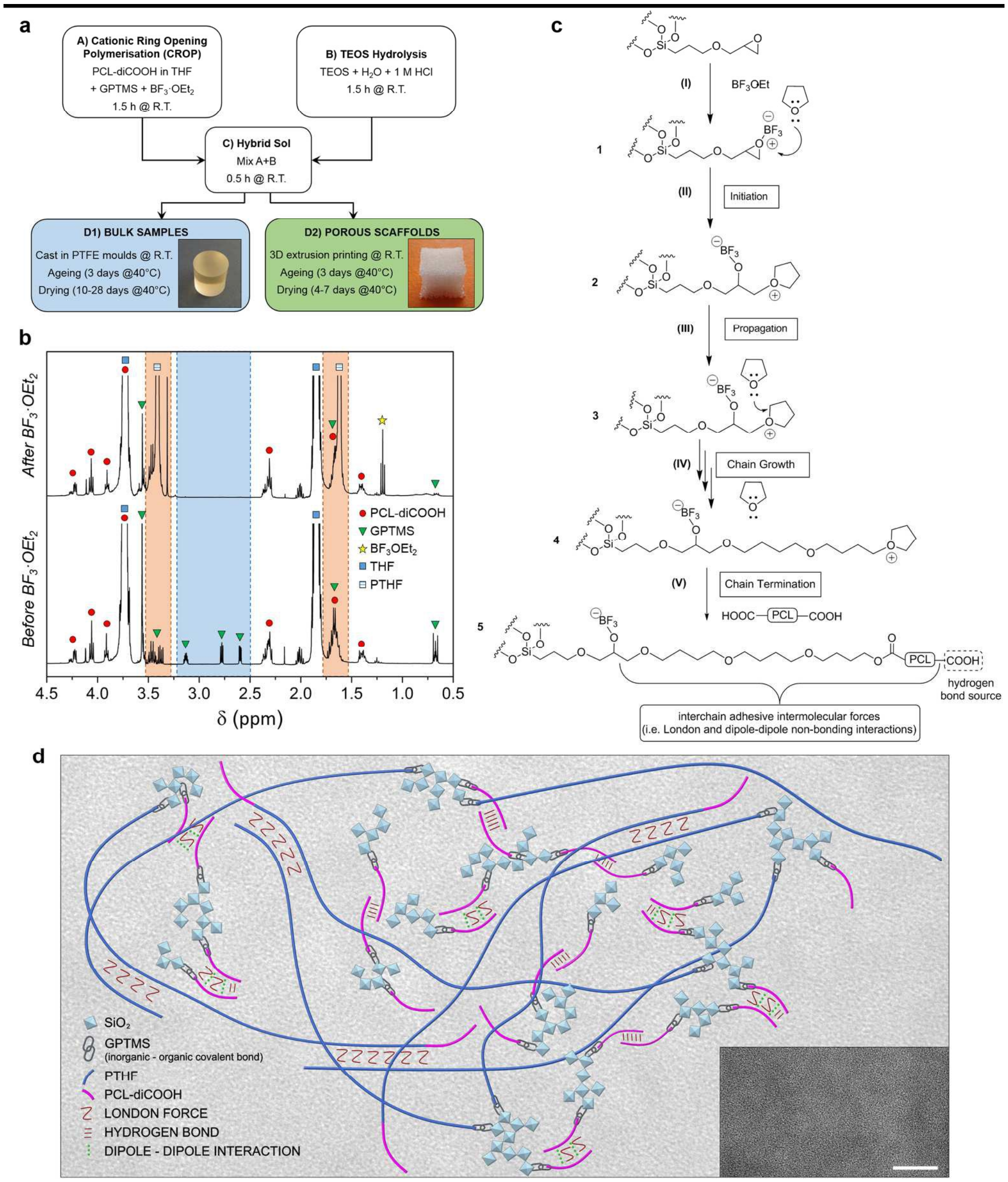

Figure 1. SiO2/PTHF/PCL-diCOOH hybrid synthesis: a, Flowchart of the synthesis protocol to prepare hybrid materials in form of monoliths (e.g. cylindrical sample (Ø = 9 mm, height = 10 mm) shown in the inset of D1 step) and 3D porous scaffolds (e.g. cubic scaffold of 8×8×8 mm shown in the inset of D2 step). b, Typical 1H-NMR spectra in CDCl3 of the solution containing organic precursors (step A in a) that show the effect of the addition of BF3·OEt2, which catalyses the CROP reaction described in c. The spectrum at the bottom, obtained before BF3·OEt2 addition, displays the characteristic peaks of the starting reagents (THF, GPTMS, PCL-diCOOH): the three peaks highlighted in the blue region (quartet at δ = 2.60 ppm, triplet at δ = 2.77 ppm and multiplet at δ = 3.13 ppm) correspond to GPTMS epoxide ring. The spectrum at the top is obtained after 1.5 h from BF3·OEt2 addition (before mixing with inorganic precursor solution): the peaks in the blue region are missing, demonstrating the completion of the opening of GPTMS' epoxide ring; this is combined with the appearance of PTHF peaks (multiplet at δ = 1.62 and triplet at δ = 3.41 ppm, orange regions), confirming the ring-opening polymerisation of THF. c, Reaction mechanism for cationic ring-opening polymerisation of THF; intermediate 5 includes the hypothesised interactions among organic components. d, Schematic of the SiO2/PTHF/PCL-diCOOH hybrid material, demonstrating the hypothesised

View Article Online
DOI: 10.1039/C8MH00027A

GPTMS-mediated covalent bonding between inorganic and organic components and interactions between polymer chains; inset: TEM image (scale bar = 50 nm) showing the homogeneity of the hybrid network at the nanoscale.

201x236mm (300 x 300 DPI)

View Article Online
DOI: 10.1039/C8MH00027A

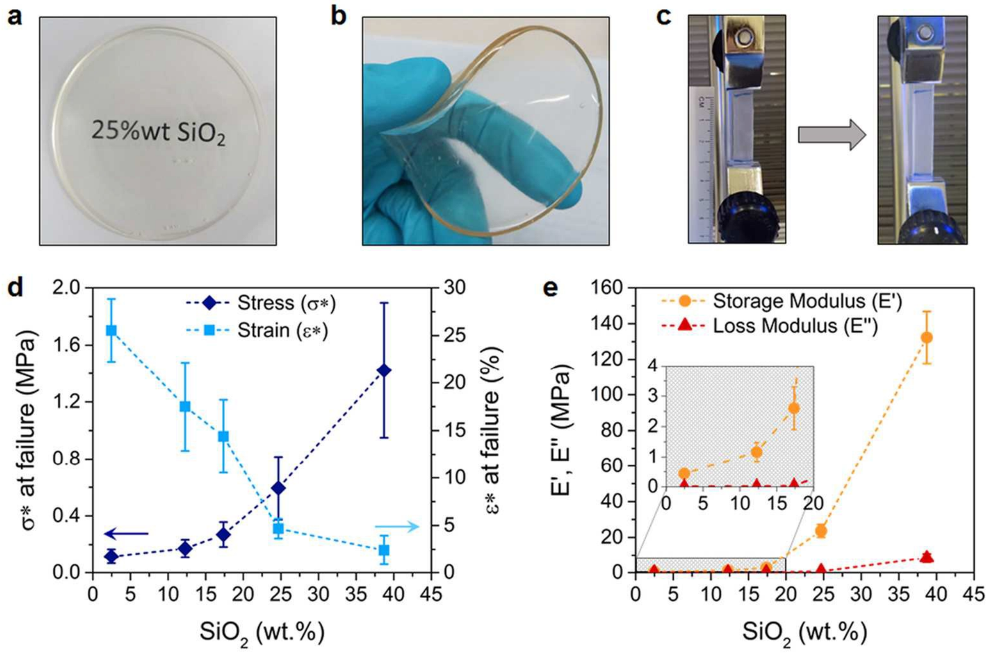

Figure 2. Mechanical properties of the SiO2/PTHF/PCL-diCOOH hybrids in the bulk state: a, Example of Si80-CL hybrid disc (Ø = 90 mm, height = 2 mm); b, Manual bending of the Si80-CL disc shown in a; c, Uni-axial tensile testing of a rectangular specimen (25×10 mm; thickness = 0.6-2 mm) manually cut from a disc; d, Mean true stress (σ*) and true strain (ε*) at failure relative to the silica content (SiO2 wt.%) as result of tensile testing; e, Storage modulus (E') and loss modulus (E'') relative to the silica content (SiO2 wt.%) as result of DMA analysis in tension on the five hybrid compositions at 1 Hz. The inset shows the magnification of the results for Si0-CL, Si60-CL and Si70-CL. (see Table 1 for correspondence SiO2 wt.% - sample acronym). Error bars in d and e represent the standard deviation.

113x75mm (300 x 300 DPI)

View Article Online
DOI: 10.1039/C8MH00027A

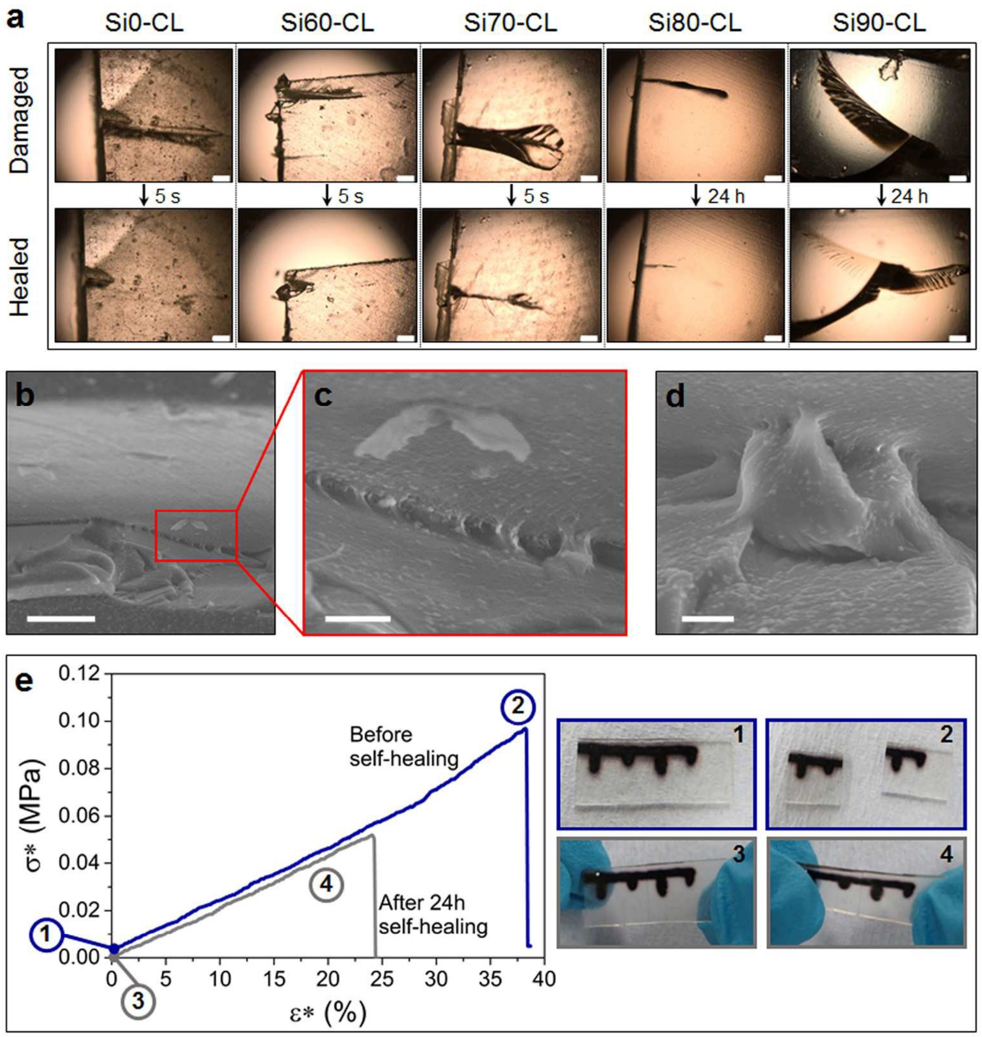

Figure 3. Autonomous and intrinsic self-healing ability: a, Optical microscope images of samples of the five hybrid compositions before creation of a defect (top) and after self-healing at R.T. (bottom). Rapid healing was observed for samples with silica content ≤ 17.4 wt.%, hence images for Si0-CL, Si60-CL and Si70-CL, were taken after only 5 s from defect creation; Si80-CL and Si90-CL showed a slower recovery, therefore images were taken after 24 h from defect creation. Scale bar = 500 μm. b-c-d, SEM images of a defect created on a Si0-CL sample and allowed to heal only partially (i.e. only the lower portions of the opposing surfaces were put in contact when re-joined) to show the bridging effect along the fractured surfaces during the self-healing process. The margins of the defects are visible in b and a magnification of the bridging is reported in c; this behaviour was confirmed also on other areas of the sample (d). Scale bars: 50 μm in b; 10 μm in c-d. e, Typical stress-strain graph of quantitative self-healing tensile test on Si0-CL (true values of stress (σ*) and strain (ε*) were considered). It shows the comparison between the curve obtained from the fresh sample ('Before self-healing') up to failure and the curve obtained from the same sample after it has been fractured into two pieces, allowed to reattach for 24 h at R.T. and humidity of ~50 % and then re-tensile tested up to failure ('After 24h self-healing'). The inserts display a typical Si0-CL sample going through this sequence.

180x189mm (300 x 300 DPI)

View Article Online
DOI: 10.1039/C8MH00027A

View Article Online
DOI: 10.1039/C8MH00027A

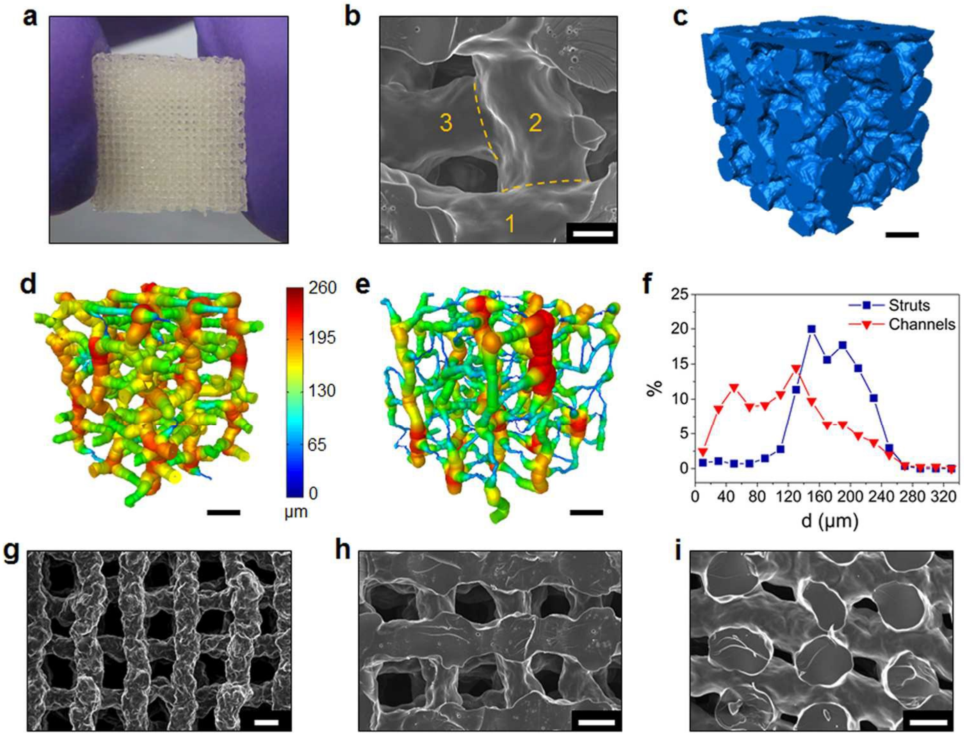

Figure 4. 3D extrusion printed scaffolds: a, Example of a scaffold (8×8×8 mm), with a grid-like 3D porous structure with aligned 90° layers (obtained from the repetition of 2 orthogonal layers, each consisting of a linear array of parallel struts); b, SEM image of a horizontal section showing the interaction among struts belonging to three different layers (identified with "1-2-3" from the outer to the inner layer): the fusion between two adjoining struts is highlighted with a dashed line; c, Example µCT image (cubic child volume, dimensions 1235 µm) of a 3D printed Si80-CL scaffold, showing 3D rendering of the struts used for the µCT image analyses in d to f; d strut and e interconnecting channel thickness visualised illustrating connectivity coloured by local diameter that fits within the structure; f, Strut and interconnecting channel size distributions calculated from d-e and binned as a percentage of the total. Scaffold porosity of 40% was calculated from these distributions (within the 42 ± 4% measured with He pycnometry); g- i, SEM images of top surface, horizontal (x-y) section and vertical (z-y) section, respectively, of a 3D printed Si80-CL scaffold. Scale bars: 100 µm in b; 250 µm in c-e; 200 µm in g-i.

128x96mm (300 x 300 DPI)

View Article Online
DOI: 10.1039/C8MH00027A

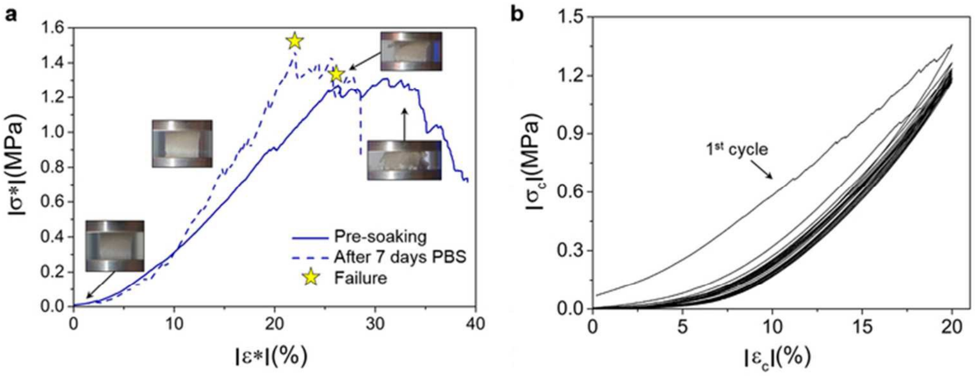

Figure 5. Compression testing on Si80-CL scaffolds: a, Typical true stress-strain graph (σ*-ε*) for a Si80-CL scaffold as prepared ("Pre-soaking") and after soaking in PBS for a week ("After 7 days PBS"). Non-linear elastomeric behaviour was recorded until failure occurred; failure was identified by the dramatic change in the trend towards a horizontal fragmented graph due to the fracture of the different scaffold layers. A stiffening of the hybrid was observed upon soaking as consequence of the degradation of the polymer component (Fig. S8). Modulus of toughness (UT), that represents the energy required to bring the sample to failure, was 142 kPa and 113 kPa for pre- and post-soaking tests, respectively; b, Typical cyclic loading conventional stress-strain (σc-εc) curves for a Si80-CL scaffold, showing its ability to recover the shape at the chosen level of strain. An anomalous first cycle is detected and is attributed to the combination of two effects: (i) The irreversible rupture of single labile struts, which are inherent in the not perfectly regular structure of the scaffold but were proven not to affect the mechanical behaviour significantly. (ii) The Mullins Effect, a characteristic featured by pure elastomers, which is mechanical stress softening due to the transformation of hard domains to soft domains that determines a decrease in stress on unloading compared to loading, giving rise to hysteresis.70, 71 This phenomenon occurs mostly in large strain cyclic loading tests in the first few cycles because of the sliding between elastomer macromolecular chains under mechanical stress, which causes the temporary elimination of hard domains present in the microstructure by removing entanglements in its internal structure. This effect is mostly recovered after the stress is removed, with the exception of some entanglements that cannot be recovered and are removed in the first few cycles.71 The other nine cycles almost perfectly overlap, with a very small hysteresis.

66x26mm (300 x 300 DPI)

View Article Online
DOI: 10.1039/C8MH00027A

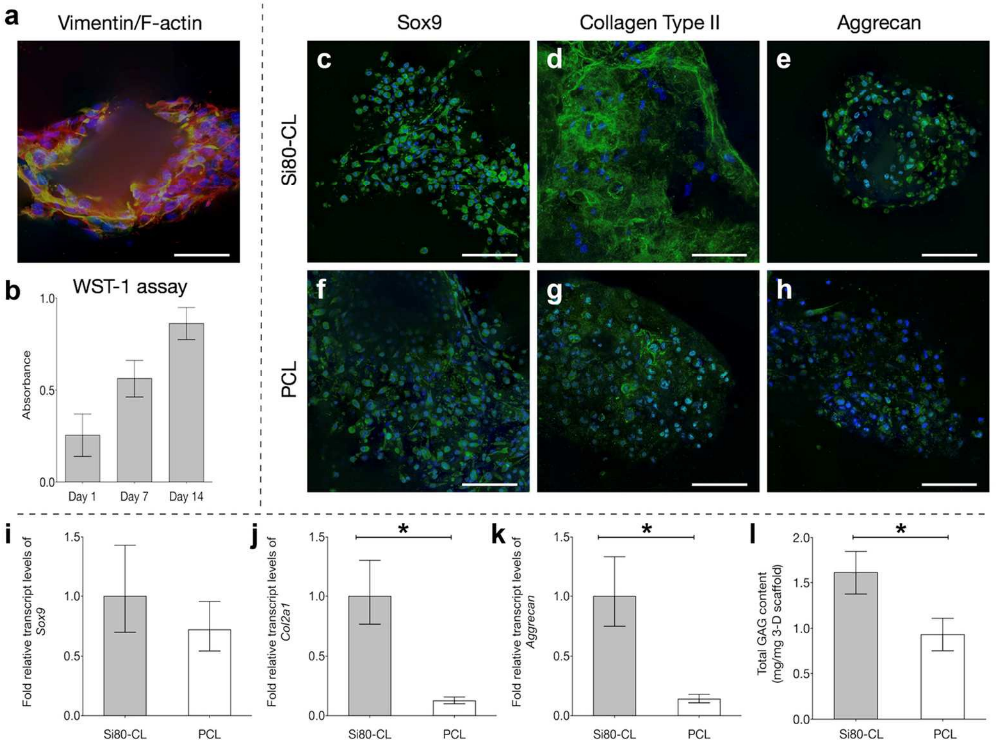

Figure 6. In vitro cell studies on Si80-CL and PCL scaffolds: a, Immunohistochemical staining of cell nuclei (DAPI, blue fluorescence), Vimentin intermediate filaments (green fluorescence) and F-actin microfilaments (red fluorescence). Cells infiltrated the pore structure within the scaffold and expression of Vimentin and F-actin is evidence of functional cell adhesion. b, WST-1 assay of ATDC5 seeded Si80-CL scaffolds cultured for up to 14 days (n = 3). The gradual increase in optical density of WST-1 solution was evidence of on-going cell survival and continual cell growth on the scaffolds. c-h, Immunohistochemical analysis of day-21 ATDC5 seeded Si80-CL and PCL constructs with markers for cartilage-related proteins. Robust chondrogenic differentiation and hyaline cartilaginous matrix formation on Si80-CL scaffolds was confirmed by staining for Sox9 (marker for chondrogenic differentiation), Aggrecan (cartilage-specific proteoglycan) and Collagen Type II (a constituent of hyaline cartilage) (c-e). Hyaline cartilaginous matrix formation appeared suboptimal in PCL scaffolds (f-h). i-k, Analysis of expression of Sox9, Col2a1 and Aggrecan using real-time qPCR (n = 3) confirmed the observations from immunohistochemistry. There was negligible Collagen Type I (fibrocartilage marker) and X (hypertrophic cartilage marker) on either type of scaffolds (Fig. S9). l, DMMB assay demonstrated that cells cultured on Si80-CL scaffolds synthesised significantly more sGAG than those on PCL scaffolds. * $p<0.05$. Scale bars in a, c-h = 100 μm. Error bars in b and l represent the standard deviation, error bars in i-k represent range (upper and lower limits) of relative gene expression.

130x99mm (300 x 300 DPI)

View Article Online
DOI: 10.1039/C8MH00027A

Bouncing and 3D Printable Hybrids with Self-healing Properties

F. Tallia, L. Russo, S. Li, A. L. H. Orrin, X. Shi, S. Chen, J. A. M. Steele, S. Meille, J. Chevalier, P. D. Lee, M. M. Stevens, L. Cipolla, J. R. Jones*

Table of Content

Novel sol-gel hybrid materials that put bounce in bioactive glass, can self-heal and can be directly 3D printed.